ACS OMEGA

Open Access

http://pubs.acs.org/journal/acsodf

Article

Depth-Resolved Temperature-Dependent Penetration of Polymyxin B in Phospholipids/Lipopolysaccharide Asymmetric Bilayers

Nicoló Paracini,* Jeremy H. Lakey, and Luke A. Clifton

Cite This: *ACS Omega* 2025, 10, 2616−2627

Read Online

ACCESS | Metrics & More | Article Recommendations | Supporting Information

ABSTRACT: The lipid matrix of the outer membrane (OM) of Gram-negative bacteria consists of a highly asymmetric lipid bilayer containing phospholipids on the inner leaflet and lipopolysaccharides (LPS) in the outer layer. The latter ensures that harmful molecules do not permeate the bacterial cell, but polymyxin B (PmB), a last-resort antibiotic, is capable of interfering with the stability of the LPS layer and overcoming the OM barrier. We have previously shown that the efficacy of PmB in disrupting isotopically asymmetric OM models (^{2}H-phospholipids and ^{1}H-LPS) is regulated by the gel-to-fluid phase transition of the LPS layer. Here, we employ fully deuterated OM models (^{2}H-phospholipids and ^{2}H-LPS) to track the temperature-dependent penetration of PmB within the model membrane by using neutron reflectometry. We use a model-independent approach to quantify PmB penetration as a function of both concentration and temperature as well as a model-dependent analysis to localize PmB in the asymmetric bilayer. By leveraging the ability of neutrons to differentiate hydrogen from deuterium in structural biology we find that PmB hijacks LPS molecules and accumulates predominantly in the hydrophobic region of lipid A.

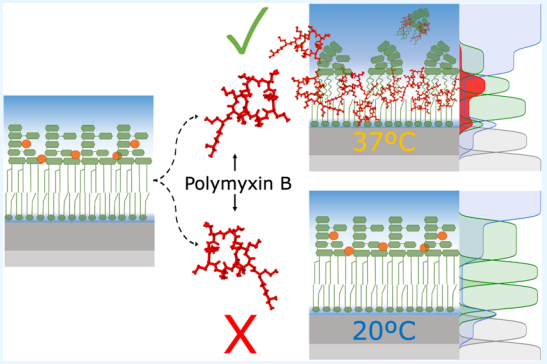

1. INTRODUCTION

Gram-negative bacteria are over-represented among antibiotic-resistant species partly due to the highly effective barrier function of their complex cell envelope.[1] Of the two lipid bilayers that surround these organisms, the outer membrane (OM) is a highly impermeable asymmetric lipid bilayer, which acts as the first line of defense against environmental threats.[2] The OM is composed of an inner leaflet of phospholipids and an outer layer of lipopolysaccharides (LPS), complex anionic glycolipids, which form a tight barrier by divalent cation-mediated cross-linking.[3] Chemically, the LPS molecule is generally divided into three distinct regions: (i) lipid A: the highly conserved hydrophobic acyl chain component, typically containing 6 saturated myristoyl (C 14:0) and lauryl (C 12:0) acyl chains held together by two phosphorylated glucosamine residues linked by a β-1,6 linkage, linked to (ii) the core oligosaccharide (OS) containing 10−12 monosaccharide units bearing anionic substituents, optionally capped by (iii) the O-antigen, a homopolymer composed of a short oligosaccharide repeating unit present in highly variable number of units per molecule.[4] LPS containing only lipid A and core OS is referred to as rough LPS while the term smooth LPS is used to designate a significantly polydisperse family of molecules (ranging from 4 up to 50 kDa) containing the O-antigen in highly variable quantities.[5] Mutations in the synthesis pathway of rough LPS in *Escherichia coli* are often introduced to obtain truncated, well-defined core OS structures, named RcLPS, RdLPS, and ReLPS (the latter corresponding to lipid A). RaLPS is the term that designates the LPS chemotype containing the complete full-length core OS.

On paper, LPS has all the characteristics of a promising target for antibiotic development: it is uniquely found in Gram-negative bacteria and it is a vital component of the first defense mechanism of these organisms.[6] Efforts to develop novel antibiotics targeting LPS have focused primarily on inhibiting LPS synthesis and transport, resulting in no approved drugs so far. LpxC, a pivotal enzyme in LPS synthesis, and LptD, part of the LPS transport chain, have been among the main targets of these approaches. Two antibiotic candidates targeting LpxC reached clinical trials but were discontinued after phase 1.[7] LPC-233, a novel compound in the same category, has demonstrated potent binding to LpxC, promising *in vitro* and *in vivo* safety profiles, oral bioavailability and bactericidal activity against a wide spectrum of Gram-negative pathogens, making it a new compelling candidate.[8] Murepavadin, an LptD inhibitor, has started phase 1 trials for oral administration after failing in phase 3 for intravenous administration.[7] Very recently, a new category of antibiotics

Received: August 19, 2024
Revised: November 23, 2024
Accepted: December 18, 2024
Published: January 14, 2025

which targets LPS transport has been proposed[9] and in this new category, Zosurabalpin, a macrocyclic peptide, has shown promising results and is about to enter clinical trials.[10]

Meanwhile, as of today, polymyxins remain the sole family of approved antibiotics that directly target LPS as an integral part of their mechanism of action.[7,11] PmB is a cationic lipopeptide used as a last-resort antibiotic in case of pan-resistant infections and it directly binds LPS and disrupts the OM in order to penetrate inside the cell and cause cell death, with a mechanism that is not yet fully elucidated.[12,13] Lipopeptide drugs such as PmB and daptomycin offer compelling therapeutic opportunities due to their potent activity against resistant strains, diverse mechanisms of action targeting structural cell components, and potential synergy with other antibiotics.[14] The bactericidal activity of PmB toward *E. coli* has been shown to be strictly temperature dependent, with little efficacy at 20 °C and potent bactericidal effects at a cell growth temperature of 37 °C.[15−17] Using a combination of neutron reflectometry (NR) and infrared spectroscopy, we have shown that in this temperature range, LPS from *E. coli* grown at 37 °C and reconstituted into asymmetric OM models, undergoes a phase transition from a gel to a fluid phase, which renders the asymmetric lipid bilayer vulnerable to the disruptive effects of PmB. Isotopic labeling of the inner and outer leaflets enabled the measurement of the individual phase transitions of both phospholipids and LPS in the system using infrared spectroscopy.[18]

NR played a key role in revealing the temperature-dependent structural effects of PmB on OM models, thanks to the unique differential sensitivity of neutrons toward hydrogen and deuterium.[19] The combination of NR with isotopically asymmetric lipid bilayers containing ^{2}H-phospholipids in the inner leaflet and ^{1}H-LPS in the outer layer is an extremely useful tool for understanding the behavior of the Gram-negative cell envelope.[5,20] However, a limitation of isotopically asymmetric ^{2}H-phospholipids/^{1}H-LPS OM models ($_{dPL/hLPS}$OMM) used in the context of studying interactions with a third component, such as an intercalating antibiotic, is the impossibility of disentangling mixing of lipids between the two leaflets from the penetration of the antimicrobial molecule.

Here, we investigate the interaction of PmB with fully deuterated asymmetric $_{dPL/dLPS}$OMM in order to elucidate the distribution of antibiotics across the deuterium-rich bilayer, yielding new insight into the activity of this important antibiotic class. We produced deuterated LPS and reconstituted it into asymmetric lipid bilayers by using a well-established combination of Langmuir−Blodgett and Langmuir−Schaefer depositions. This provided a platform to assess temperature and concentration-dependent effects of PmB on the $_{dPL/dLPS}$OMM and, crucially, to resolve the temperature-dependent penetration of PmB into the lipid bilayer from a structural point of view.

2. MATERIALS AND METHODS

2.1. Production and Characterization of Deuterated LPS. *2.1.1. Media.* For deuterated LPS production, a minimal medium was prepared according to Meilleur et al.[21] The media prepared in deuterium oxide (D_2O) was sterilized by filtration and no antibiotic was added.

2.1.2. Cell Growth. *E. coli* K12 BW25113, the parent strain of the Keio collection, was used to extract deuterated RaLPS as it produces rough LPS with a complete core oligosaccharide region. Deuteration of cells was carried out as described by Meilleur et al.[21] with some modifications. Cells were first adapted to grow in the presence of deuterium oxide (D_2O) by initially inoculating a single colony of cells grown on Agar into 5 mL minimal media made containing 25% D_2O and 75%H_2O (v:v). After an overnight growth at 37 °C, 0.1 mL of culture was used to inoculate a minimal media solution made with 50% H_2O and 50% D_2O, and the cells were grown overnight. The process was iterated by successively inoculating the resulting cultures in media containing 75, 90, and 98% D_2O over the course of 3 days. Three × 250 mL flasks containing 50 mL of minimal media made with 98% D_2O were then inoculated with 1 mL of the 98% D_2O-adapted cells and grown overnight. The cultures were harvested by centrifugation at 2350*g* at room temperature, resuspended in 10 mL of fresh 98% D_2O minimal media, and used to inoculate a 1.5-L Minifors1 fermentation vessel (INFORS) containing 1 L of 98% D_2O minimal media at 37 °C. The fermenter was set in cascade mode to maintain a fixed pO2 of 40% by adapting the stirring speed between 200 and 1000 rpm. The pH was not controlled. Cell growth was monitored by measuring the OD_{600} nm in a UV-spectrophotometer (Shimadzu) until it reached at least 10.0. The cells were then harvested by centrifugation at 8000*g* for 10 min at 4 °C. The cell pellet was then washed twice with Nanopure water and freeze-dried until all the water was removed.

2.1.3. LPS Extraction. Rough LPS was extracted following the method by Galanos et al.[22] The freeze-dried cell pellets were gently homogenized in phenol/$CHCl_3$/petroleum ether 2:5:8 (v/v/v) (PCP) using 10 mL for every gram of dry cells for three h with gentle stirring. To prepare the PCP solvent, pure $CHCl_3$ was mixed with a commercial solution of $CHCl_3$, phenol, isoamyl alcohol 49.5:49.5:1 (v/v/v), and petroleum ether (boiling point 40−60 °C), all purchased from Sigma-Aldrich. The cell suspension was centrifuged in glass tubes at 2350*g* for 15 min. The supernatant was kept, and the pellet was rehomogenized in the organic mixture for three more hours. The supernatant from each extraction was pooled and vacuum filtered by using coarse filter paper. The filtered solution was then transferred to a glass round-bottom flask, and the chloroform and petroleum ether were removed by rotary evaporation at 55 °C for 1 h. LPS was precipitated out of the remaining phenol solution by dropwise addition of a 1:1 solution of diethyl ether and acetone (v/v) until a white precipitate formed. The solution was left overnight at room temperature to allow for complete precipitation. The precipitate was centrifuged at 2350*g* for 15 min and washed three times with water-saturated phenol equilibrated in a separating funnel to avoid excess water, followed by three washes of diethyl ether to remove traces of phenol. The obtained white pellet was dried in a stream of air and used with no further purification.

2.1.4. Thin Layer Chromatography. Thin layer chromatography (TLC) analysis of hydrogenous and deuterated lipid A and RaLPS species was performed on silica-coated plates (Sigma-Aldrich) and eluted with a mobile phase containing $CHCl_3$, MeOH, H_2O 60:39:1 (v/v/v) Lipid A was obtained from hydrogenous and deuterated RaLPS by mild acid hydrolysis as described by Henderson et al. (Henderson et al., 2013). Fifteen μL of a $CHCl_3$ 1 mg/mL solution of lipid A were spotted with a glass capillary on the silica plate while the same amount of RaLPS was spotted from a $CHCl_3$, MeOH, H_2O 60:39:1 (v/v/v). The spots were dried under a stream of air, and the plate was placed in the TLC tank equilibrated with

https://doi.org/10.1021/acsomega.4c07648
ACS Omega 2025, 10, 2616−2627

the mobile phase vapors until the solvent front reached a distance of 1 cm from the top of the plate. The plate was dried in the fume hood and immersed in a 10% ethanolic solution of H_2SO_4 for 1 min, then dried and charred using a Bunsen burner until the spots developed.

2.1.5. Sodium Dodecylsulfate Polyacrylamide Gel Electrophoresis. Analysis of LPS by sodium dodecylsulfate poly(acrylamide gel electrophoresis) (SDS PAGE) followed the standard protocol based on a two-part discontinuous acrylamide gel described by Laemmli.[23] The resolving (lower) gel contained a buffer made of 375 mM Tris-HCl pH 8.8, 0.1% (w/v) SDS and 12% (v/v) acrylamide. 10% ammonium persulfate and tetramethylethylenediamine (TEMED) were added to catalyze the polymerization reaction, and a layer of water-saturated butanol was applied to the top of the solution contained in the glass cast to obtain a defect-free interface. Once the lower gel had set, the butanol layer was rinsed away and the stacking gel was applied. This contained a buffer made of 125 mM Tris-HCl pH 6.8, 0.1% (w/v) SDS, and 4% (v/v) acrylamide and was polymerized the same way as the lower gel after a comb was inserted in the gel. 10 μL of the sample were mixed 1:1 with a loading dye containing 15% (v/v) glycerol 125 mM Tris-HCl, 2% (v/v) SDS 0.1% (w/v) bromophenol blue, 1% (v/v) mercaptoethanol pH 6.8. 10−20 μL of sample-dye mix were loaded into the wells of the loading gel. The gel was resolved using 180 V current in a buffer containing 25 mM Tris-HCl, 192 mM glycine, 0.1% (w/v) SDS pH 8.0 in a mini PROTEAN tetra cell (Bio-Rad) and bands were visualized by silver staining.

2.1.6. Silver Staining. LPS bands were visualized on the polyacrylamide gels using silver staining.[24] Gels were stained by using a silver stain kit (Bio-Rad) according to the manufacturer protocol with some modifications. Briefly, once the gel was run, it was left overnight in 100 mL of a solution containing 50 mL of MeOH, 30 mL of deionized water, 10 mL of glacial acetic acid, and 10 mL of the fixative enhancer provided with the kit. After the overnight incubation, the gel was thoroughly rinsed with deionized water and incubated with a spatula of Chelex-100 resin for 20 min. The staining solution was prepared by mixing 0.625 g of the development accelerator reagent in 12.5 mL of distilled water and, separately, 8.75 mL of distilled water with 1.25 mL of silver stain complex reagent, 1.25 mL of reduction moderator solution, and 1.25 mL of image development reagent. Before staining the gel, the Chelex-100 resin was removed, and the gel was thoroughly rinsed with deionized water. The development accelerator solution was mixed with the remaining staining solution just before adding the mix to the gel, which was left rocking until the bands developed. The staining was stopped by adding 5% acetic acid to the staining solution before the background developed a dark color. Gels were imaged on a Gel Doc XR+ (Bio-Rad) gel.

2.1.7. Transmission Infrared Spectroscopy. IR absorption of deuterated LPS was measured in transmission mode, with the beam passing directly through the sample. A 1 mg/mL suspension of deuterated LPS in $CHCl_3$, MeOH, H2O 60:39:1 (v/v/v) was spread on a calcium fluoride window, and the solvent was allowed to evaporate under a nitrogen stream and left for 2 h under vacuum to remove traces of solvent. Measurements were taken with a deuterated-triglycin-sulfate (DTGS) detector on a Nicolet iS50 spectrometer (Thermo Fischer) summing 64 spectra per sample.

2.2. Formation of Asymmetric Phospholipids/LPS Bilayers and NR Experimental Set-up. Asymmetric outer membrane models (OMM) containing d_{62}DPPC in the inner leaflet and deuterated RaLPS in the outer leaflet ($_{dPL/dLPS}$OMM) were assembled as described previously,[18,25−27] using sequential Langmuir−Blodgett and Langmuir−Schaefer depositions of lipid monolayers onto the major face of a 50 × 80 × 15 mm^3 silicon crystal polished to an rms roughness of <5 Å. The sample environment used for the NR measurement, including solid−liquid cells, HPLC pump for solvent exchange, and water bath arrangement is described in detail by Clifton et al.[19] The buffer used in the experiments was 20 mM HEPES pH/pD 7.4 supplemented with 5 mM $CaCl_2$ and the flow rate of solvent exchange was 1 mL/min. PmB was incubated with the OMM for 20 min before measuring in each condition of temperature and concentration.

2.3. Neutron Reflectometry Measurements. Neutron reflectometry (NR) measurements were performed at the ISIS Muon and Neutron source (Didcot, UK) on the OFFSPEC reflectometer. NR was measured at two incidence angles θ of 0.7 and 2.0° using neutrons with a wavelength λ between 1.5 and 14.5 Å, yielding a Q range between 0.012 and 0.35 $Å^{-2}$ where Q is defined as

$$Q = 4\pi\frac{\sin\theta}{\lambda} \tag{1}$$

Data was reduced using the Mantid software[28] by dividing the reflected intensity by a transmission measurement to obtain the reflectivity as a function of Q.

2.4. Analysis of Neutron Reflectometry Data. Neutron reflectivity data sets were analyzed using the refnx python package[29] which leverages Bayesian inference and optimization techniques for robust modeling, using the script available on GitHub[30] and Zenodo.[31] Parameter estimation was first performed using the differential evolution algorithm, a global optimization method that is effective for complex parameter landscapes. Markov Chain Monte Carlo (MCMC) sampling was then employed to probe the posterior distribution of the model parameters. This process allowed for comprehensive uncertainty quantification, providing 68% confidence intervals of the obtained values, as well as highlighting potential parameter correlations. The posterior distribution, obtained from MCMC samples, was visualized using corner plots shown in Figure S2, which provided a detailed view of the parameter space, highlighting regions of high probability and parameter correlations. As a figure of merit for the goodness of fit, we used the global reduced χ^2 value calculated as

$$\chi^2_{\text{reduced}} = \frac{\chi^2}{\text{degrees of freedom}} = \frac{\chi^2}{N - p} \tag{2}$$

Where N is the number of experimental data points and p is the number of fitted parameters in the model.

The OMM was modeled as a series of four slabs representing in order, moving away from the substrate, the phospholipid headgroup, the phospholipid tails, the LPS tails, and the LPS headgroup (core OS). The two slabs of the phospholipid leaflet were modeled using a single area per molecule (APM) parameter to parametrize the lipid molecules based on their molecular volumes, obtained from Armen et al.[32] LPS tails and head groups were modeled as two independent slabs due to the heterogeneity of the molecules. A single hydration value was used for the lipid tails, assuming

https://doi.org/10.1021/acsomega.4c07648
ACS Omega 2025, 10, 2616−2627

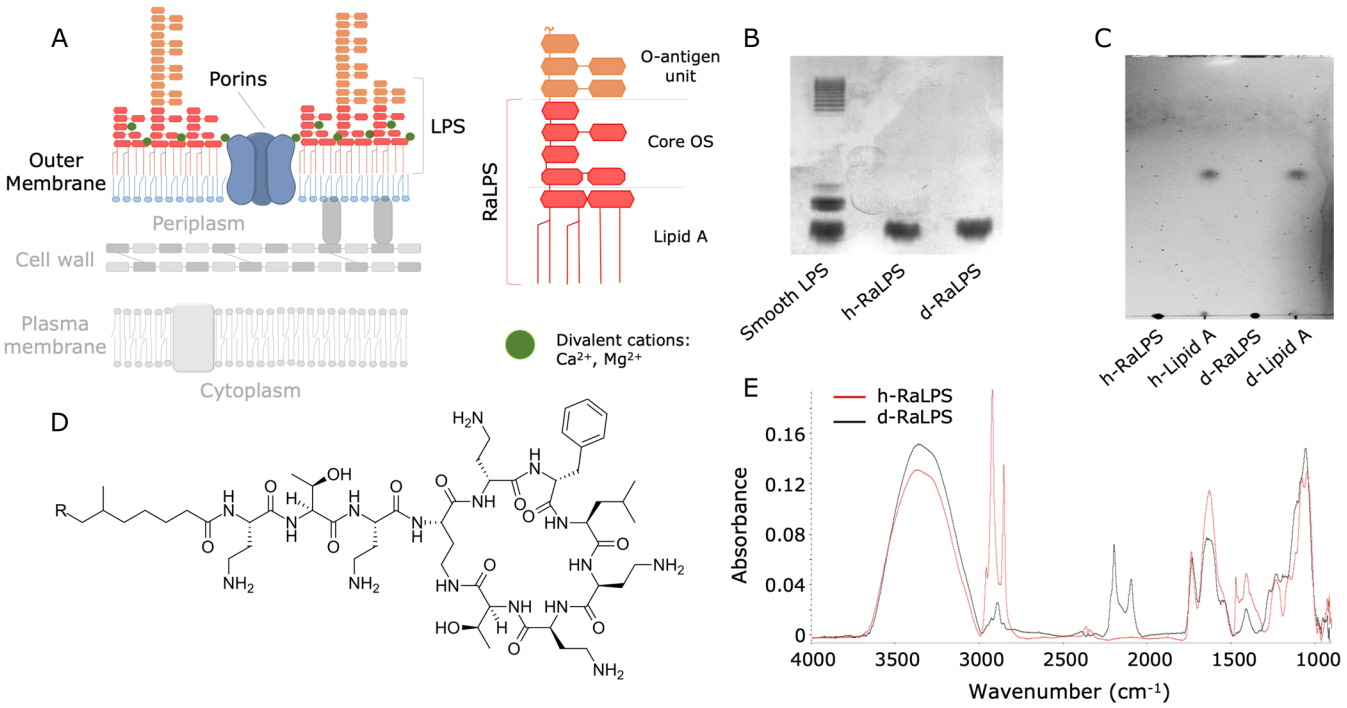

Figure 1. Characterization of deuterated LPS. (A) Cartoon representation of the OM and schematic of LPS (B) SDS PAGE of smooth LPS standard (chemotype O111), RaLPS standard (from strain EH100), and deuterated LPS produced in this work. (C) TLC elution profiles of RaLPS standard, deuterated RaLPS, and their respective lipid A components obtained via acid hydrolysis. (D) Chemical structure of polymyxin B. R = CH3 is polymyxin B1, R = H is polymyxin B2, and (E) Comparison of infrared spectroscopy signal from h-RaLPS standard and d-RaLPS.

that water present in this region is due to defects that span the whole lipid bilayer. Each one of the four slabs modeling the head groups and tail regions of the $_{dPL/dLPS}$OMM is described by layer thickness, roughness, and SLD values which can be used to reconstruct the volume fraction profile of the components across the interface as well as the volume fraction of water penetrating in the different regions of the sample. The model was set up to minimize the number of free parameters fitted by sharing common parameters for multiple data sets. The roughness of the bilayer was assumed to propagate from one leaflet to the other and was therefore constrained to vary uniformly across the 4 regions of the bilayer and described by a single value. This approach is typical in so-called contrast variation NR where the sample is measured multiple times against a background solution composed of different D_2O/H_2O mixtures and the resulting data sets are constrained to share the same values of material scattering length density (SLD), layer thickness and roughness values, but are allowed individual values for the SLD of the aqueous solution,[19] where the SLD is given by

$$\mathrm{SLD} = \frac{\sum_{i=1}^{n} b_c}{v_m} \quad (3)$$

where b_c is the coherent scattering length of the ith atom in a given molecule and v_m is the molecular volume. Building on this approach, we constrained the fit from two independent deuterated bilayers, each one in three conditions: (i) $_{dPL/dLPS}$OMM at room temperature, (ii) $_{dPL/dLPS}$OMM at 37 °C and (iii) $_{dPL/dLPS}$OMM at 37 °C in the presence of 100 μg/mL PmB. Each condition was measured in three solution contrasts, H_2O, SMW (38% H_2O) and D_2O yielding a total of 18 reflectivity curves. A more detailed description of the model parametrization is given in the notebook available on GitHub which allows to reproduce the analysis and generate the plots displayed here.[30]

The area under the reflectivity curves was calculated by using trapezoidal integration. To estimate the uncertainty in the area, we considered the intensity values along with their associated error bars, which represent the uncertainty in the measured intensities. The upper and lower bounds of the intensity, obtained by either summing or subtracting the error from the intensity, were used to create an error envelope for each curve. We then calculated the areas for three cases: the original intensity, the upper bound (intensity + error), and the lower bound (intensity − error). The standard deviation of these three integrals is reported here as the uncertainty in the total area, providing an estimate of the error for the integrated intensity.

3. RESULTS

3.1. Deuterated RaLPS Characterization. Deuterated RaLPS, from now on referred to as d-LPS, was produced by adapting *E. coli* K12 to grow in a heavy water medium and purified according to the procedure described in the methods section. The characterization of the purified LPS extract is shown in Figure 1. The SDS PAGE profile of d-LPS shows a single band with a molecular weight comparable to that observed for commercial RaLPS from *E. coli* EH100 (Figure 1a). The comparison with smooth LPS from *E. coli* O111 shows that both rough h- and d-LPS lack the additional bands corresponding to smooth LPS species containing the O-antigen, which form the well-known ladder-like pattern.[33] Acid hydrolysis of LPS releases the lipid A moiety, which can be visualized by TLC (Figure 1b). Both h-lipid A and d-lipid A displayed an identical retention factor of the single species detected in each sample, suggesting comparable acylation

https://doi.org/10.1021/acsomega.4c07648
ACS Omega 2025, 10, 2616−2627

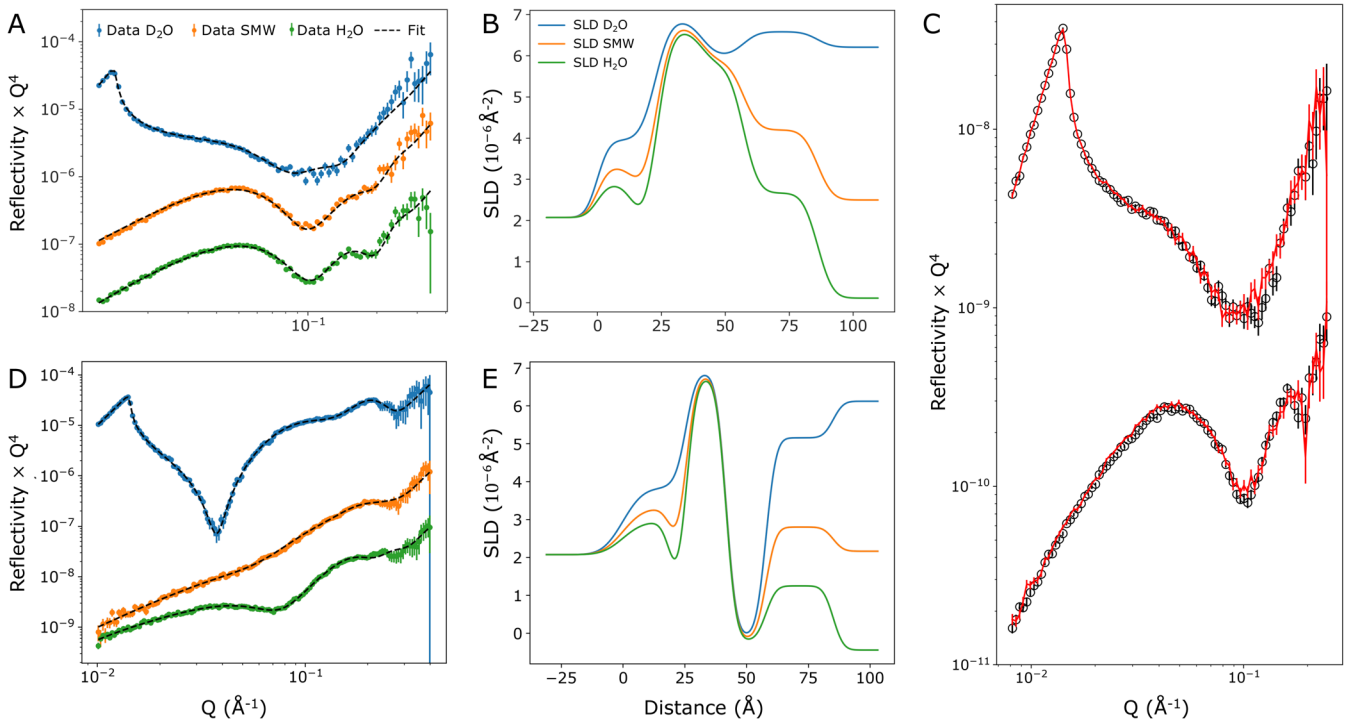

Figure 2. Characterization of $_{dPL/dLPS}$OMM and PmB effect at RT. (A) Neutron reflectivity data (points) collected under three isotopic solution contrasts from the asymmetric lipid bilayer containing deuterated d_{62}DPPC in the inner leaflet and deuterated RaLPS in the outer leaflet. Constrained fits to the reflectivity curves (dashed lines). Data sets are offset vertically for clarity. (B) SLD profiles describing the interfacial structure obtained from the fits shown in A. (C) $_{dPL/dLPS}$OMM measured in D_2O (top) and H_2O (bottom) before (empty circles) and after (red lines) the addition of 100 μg/mL PmB at room temperature. No significant effects were observed. Data sets are offset vertically for clarity. (D, E) Reflectivity and SLD profiles of the isotopically asymmetric $_{dPL/hLPS}$OMM, which highlight the high asymmetry of the bilayer obtained using the Langmuir−Blodgett/Langmuir−Schaefer deposition method, adapted from Paracini et al.[18] for comparison.

levels of the two major lipid A species. The deuteration level of d-LPS was assessed using infrared spectroscopy (IR). Although IR is not a quantitative method, the spectrum of d-LPS clearly shows the presence of the C−^{2}H stretching vibrations between 2250 and 2050 cm^{-1} lacking in the h-LPS spectrum which instead shows absorption in the 3000−2800 cm^{-1} corresponding to the C−^{1}H stretching vibrations. d-LPS shows a residual C−^{1}H signal as the carbon source in the growth medium (i.e., glycerol) was not deuterated, thus the deuteration level is below 100% (Figure 1c). For a comparison the IR signal of hydrogenous and tail-deuterated synthetic d_{62}DPPC is shown in Supporting Figure S1.

3.2. Neutron Reflectometry Characterization of $_{dPL/dLPS}$OMM and PmB Interaction at Room Temperature. d-LPS was reconstituted into $_{dPL/dLPS}$OMM using sequential Langmuir−Blodgett and Langmuir−Schaefer transfer of d_{62}DPPC and d-RaLPS monolayers and neutron reflectivity profiles were measured on the asymmetric lipid bilayers under three isotopic solution contrasts (Figure 2a).

The constrained fits of the three reflectivity data sets to a common model of the interface (see Section 2) yields the scattering length density (SLD) profile of the $_{dPL/dLPS}$OMM (Figure 2b) which describes how the neutron refractive index changes across the sample, perpendicularly to the interface. The resulting parameters obtained from the fit, reported in Table 1, describe a high-coverage lipid bilayer with 4 ± 1% of the volume in the hydrophobic region occupied by water, while in the inner and outer headgroup regions, the volume fraction of water (hydration) was 49 ± 3 and 30 ± 1% respectively. The SLD values obtained for the tail region of LPS is (6 ± 0.04) × 10^{-6} Å^{-2}, marginally lower than 6.87 × 10^{-6} Å^{-2} calculated for the inner leaflet of synthetic d_{62}DPPC confirming the high level of deuteration of d-LPS. Unlike in the case of isotopically asymmetric $_{dPL/hLPS}$OMM, lipid asymmetry cannot be inferred directly from the different SLDs of the hydrocarbon region (Figure 2d,e). However, the difference in size and SLD of the inner and outer headgroup regions clearly shows a high degree of lipid asymmetry, which combined with our previous results on the formation of asymmetric phospholipids:LPS bilayers indicates that the perdeuterated bilayer displays near-complete asymmetry. The extension of the outer headgroup, i.e., the core OS, resulted to be 29.2 ± 0.3 Å in agreement with values reported previously for RaLPS.[25,26] Overall the data obtained on the $_{dPL/dLPS}$OMM were in excellent agreement with the expected molecular structure of an asymmetric perdeuterated phospholipids/LPS bilayer.

The addition of 100 μg/mL of PmB to the $_{dPL/dLPS}$OMM at room temperature did not affect the reflectivity signal measured both in H_2O and in D_2O indicating the lack of any significant PmB effects on the model membrane and confirmed what we had previously reported[18] (Figure 2c).

3.3. Effect of Temperature on PmB Binding to $_{dPL/dLPS}$OMM: Model-Independent Analysis. The intensity of the neutron reflectivity signal is proportional to the difference between the SLD of the sample at the interface and the SLD of the surrounding media. In the case of the perdeuterated $_{dPL/dLPS}$OMM this difference is maximized when measured against hydrogenous buffer prepared in H_2O. Therefore, alterations of the reflectivity against the H_2O

https://doi.org/10.1021/acsomega.4c07648
ACS Omega 2025, 10, 2616−2627

Table 1. Neutron Reflectometry Model Parametrization and Fitted Values[a]

A

	$_{dPL/dLPS}$OMM @ RT (Sample 1 + Sample 2)			
Layer	Thickness (Å)	SLD (10^{-6}Å^{-2})	Hydration (%)	Roughness (Å)
PC Heads	6.6 ± 0.3†	1.88	49 ± 3	4.7 ± 0.3
PC Tails	18.2 ± 0.9†	6.87	4 ± 1	
LPS Tails	16.2 ± 0.7	6.0 ± 0.04		
LPS Core OS	29.0 ± 0.3	6.81 ± 0.02‡	30 ± 1	

	$_{dPL/dLPS}$OMM @ 37C (Sample 1 + Sample 2)			
Layer	Thickness (Å)	SLD (10^{-6}Å^{-2})	Hydration (%)	Roughness (Å)
PC Heads	6.4 ± 0.3†			4.4 ± 0.4
PC Tails	17.8 ± 0.9†		4 ± 1	
LPS Tails	14.0 ± 1.1	5.7 ± 0.07		
LPS Core OS	29.2 ± 0.4		43 ± 2	

	$_{dPL/dLPS}$OMM @ 37C + 100 μg/ml PmB (Sample 1)				
Layer	Thickness (Å)	SLD (10^{-6}Å^{-2})	Hydration (%)	Roughness (Å)	PmB VF (%)
PC Heads		§		3.9 ± 0.8	17.7 ± 11.8
PC Tails		§	7 ± 1		11.9 ± 1.8
LPS Tails		§			31.9 ± 3.7
LPS Core OS	17.2 ± 1	§	67 ± 4		3.0 ± 1.8

	$_{dPL/dLPS}$OMM @ 37C + 100 μg/ml PmB (Sample 2)				
Layer	Thickness (Å)	SLD (10^{-6}Å^{-2})	Hydration (%)	Roughness (Å)	PmB VF (%)
PC Heads		§		3.5 ± 0.5	31.5 ± 11.1
PC Tails		§	12 ± 1		6.8 ± 1.0
LPS Tails		§			23.4 ± 2.9
LPS Core OS	20.2 ± 1	§	68 ± 3		1.9 ± 1.0

B

	Fixed Parameters	
Parameter	Value	Units
PC Heads Volume	320.9	Å^3
PC Tails Volume	892.2	Å^3
PC Heads $\sum b$	6.04	10^{-4} Å
PC Tails $\sum b$	61.30	10^{-4} Å
SiO_2 SLD	3.47	10^{-6} Å^{-2}
Si SLD	2.07	10^{-6} Å^{-2}
PmB SLD	2.22‡	10^{-6} Å^{-2}

	Derived Parameters	
Parameter	Value	Units
PC Heads SLD	1.88	10^{-6} Å^{-2}
PC Tails SLD	6.87	10^{-6} Å^{-2}

	Fitted Parameters	
Parameter	Value	Units
PC APM RT	49 ± 2.4	Å^2
PC APM 37C	50.2 ± 2.5	Å^2

C

Layer	PmB VF (%)
PC Heads	25.0 ± 8.1
PC Tails	9.5 ± 0.7
LPS Tails	27.5 ± 2.5
LPS Core OS	2.5 ± 1.1

[a](A) diagram of the layer structure of the lipid bilayers showing the parameters describing each layer under the different conditions. In blue parameters that were allowed to fit, in white parameters fixed to the calculated value, and in green the parameters that shared the same value with the preceding condition as indicated by the connecting arrows. (B) Additional fixed parameters used in the model, including the scattering lengths and molecular volumes of d_{62}DPPC and the area per molecule (APM) values fitted in the model. (C) Average of the PmB volume fractions obtained from samples 1 and sample 2. †Values obtained by dividing the molecular volume by the fitted value of the APM at RT and 37 °C, respectively; errors are retrieved from the propagation of the APM uncertainties. ‡SLD value of the core OS and PmB in D_2O, accounting for exchangeable hydrogen atoms as deuterium atoms. In the fits, these values are adjusted according to the volume fraction of D_2O present in each solution contrast considering that the ratio between the SLD of both PmB and core OS in H_2O to the SLD in D_2O is 0.5. §The SLD of the nominal components of these regions was constrained to the values of the bilayer at 37 °C and the global SLD of each layer modified only by the volume fraction of PmB in each region.

background provide direct insights into changes in the composition of the bilayer at the interface. Figure 3a shows the reflectivity of the $_{dPL/dLPS}$OMM at room temperature, after heating to 37 °C and after the addition of 100 μg/mL of PmB at 37 °C. Both processes result in a major intensity decrease in the reflectivity signal, quantified in the inset as the reduction in the area under the curves, normalized to the reflectivity at room temperature. From the data, it is evident how heating induces a structural change in the bilayer which in turn enables the interaction of PmB with the OMM. Unlike what was observed at room temperature in fact (Figure 2c), the addition of PmB at 37 °C caused a major shift in the reflectivity signal, confirming the central role of temperature for this interaction.

To complement the data obtained on the effect of 100 μg/mL of PmB to the $_{dPL/dLPS}$OMM, a second sample was first heated to 37 °C, and the reflectivity signal in H_2O monitored as increasing amounts of PmB were titrated onto the asymmetric bilayer (Figure 3b). Five μg/mL PmB were sufficient to cause a reduction of ∼10% in the intensity of the reflectivity signal which further decreased by an additional ∼10% as the total concentration was raised to 10 μg/mL (Figure 3b inset). The extent of the reduction in the reflectivity signal progressively attenuated as the concentrations of the antimicrobials gradually increased. The intensity decreased by ∼10% at 50 μg/mL with only a marginal decrease when going from 50 to 100 μg/mL.

Finally, the effect of temperature was assessed by measuring the reflectivity as a function of temperature on a $_{dPL/dLPS}$OMM in the presence of 100 μg/mL of PmB to investigate the structural changes induced by PmB on the model membrane upon stepwise heating from 20 to 44 °C. Heating the $_{dPL/dLPS}$OMM in the presence of the antimicrobial resulted in a progressive decrease in the intensity of the reflectivity signal (Figure 3b). A plot of the area under the reflectivity curve as a function of temperature shows a sigmoidal trend, typical of phase transitions. The midpoint of the sigmoid was found to be around 32 °C, where the inflection point indicates that around this temperature the change in the signal intensity is maximal (Figure 3c inset). The quantitative analysis of the intensity drop is in excellent agreement with the first two samples analyzed, with virtually the same loss of intensity at 37 °C in the presence of 100 μg/mL PmB, showing good reproducibility of the process.

3.4. Effect of Temperature on PmB Binding to $_{dPL/dLPS}$OMM: Model-Dependent Analysis. To obtain detailed structural information on the sequential effects of heating and PmB interaction with the $_{dPL/dLPS}$OMM, neutron reflectivity was measured in three solution contrasts for the samples shown in Figure 3a and b at 20 °C, at 37 °C and at 37 °C in the presence of 100 μg/mL PmB. This generated 18 data sets, nine for each sample, which were fitted to a unified model of the interface (Figure 4a,b) designed to minimize the number of free parameters in the global fit while providing robust information on the structural changes taking place in the sample and on the penetration of PmB in the $_{dPL/dLPS}$OMM (Figure 4c–f).

Compared to the results of the fits at 20 °C, presented earlier, heating the $_{dPL/dLPS}$OMM to 37 °C affected significantly only the outer LPS leaflet, while the dDPPC leaflet, within error, remained unchanged, with an area per molecule of 49.0

https://doi.org/10.1021/acsomega.4c07648
ACS Omega 2025, 10, 2616−2627

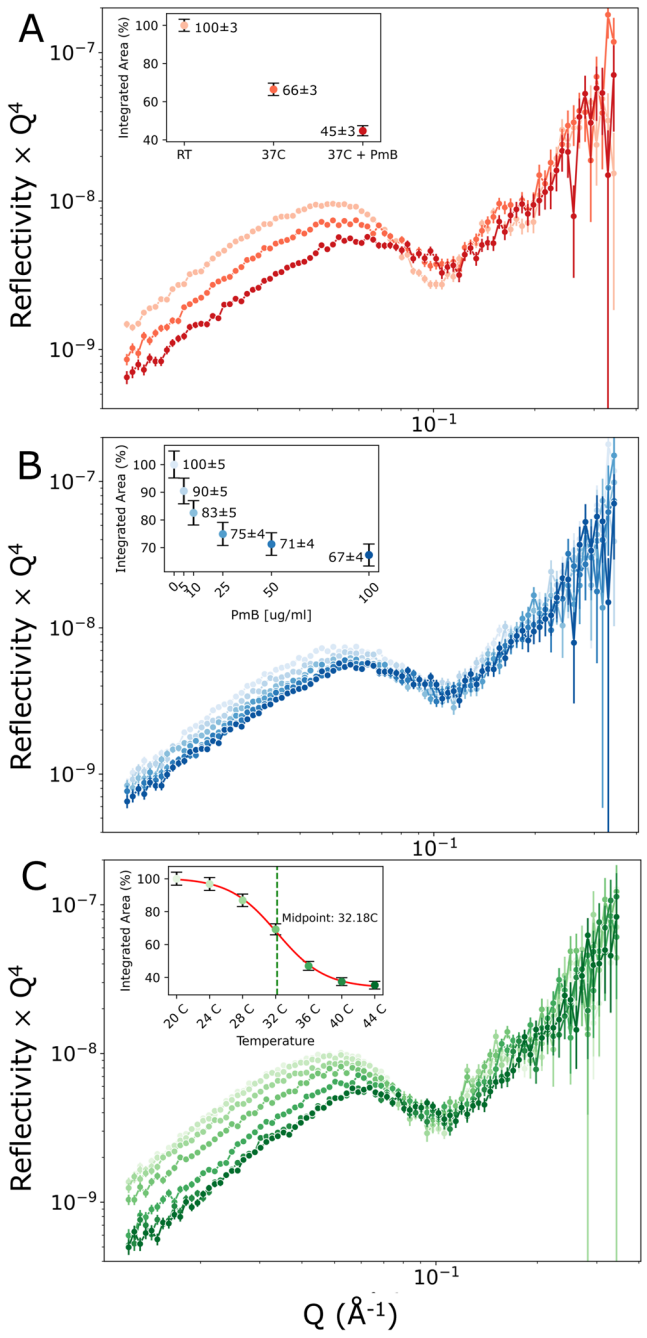

Figure 3. Effect of temperature and PmB concentration. (A) NR curves measured on $_{dPL/dLPS}$OMM in H_2O at room temperature (light orange), after heating to 37 °C (orange), and after injection of 100 μg/mL PmB (red). The inset shows a plot of the area under the curves normalized to the curve at RT. (B) $_{dPL/dLPS}$OMM at 37 °C in the presence of increasing amounts of PmB, namely 0, 5, 10, 25, 50, and 100 μg/mL PmB. The inset shows the decrease in the area under the curve as a function of PmB concentration, normalized to the curve at 37 °C and 0 μg/mL PmB (100%). (C) $_{dPL/dLPS}$OMM in the presence of 100 μg/mL of PmB at increasing temperatures, from 20 to 44 °C, in 4 °C steps (light to dark green). In the inset, the plot of the area under the curves at each temperature step normalized to the curve measured at 20 °C and fitted to a sigmoid function with the midpoint displayed. Error bars in all insets are associated with the uncertainty of the neutron reflectometry measurements.

± 2.4 Å^2 at 20 °C and 50.2 ± 2.5 Å^2 at 37 °C. The lipid A region of the LPS leaflet decreased both in thickness and in SLD going from 16.2 ± 0.7 to 14.0 ± 1 Å and from (6.0 ± 0.04) × 10^{-6} to (5.7 ± 0.07) × 10^{-6} Å^{-2}, respectively, while retaining a coverage of <95%. Interestingly, the water content in the core OS region increased by ∼13% from 30 ± 1 to 43 ± 2%. Overall, the changes observed in the LPS leaflet are in agreement with the transition of this region from a gel state to a less dense fluid phase, which we have previously reported and characterized in this temperature range for $_{dPL/hLPS}$OMM.[18] In particular, the reduction in the SLD of the LPS tail region observed here is a clear sign of the density decrease that occurs when the alkyl chain region of lipids melts, a phenomenon comprehensively characterized by NR studies on model deuterated lipid membranes[34] As shown in the titration data (Figure 3b) addition of increasing amounts of PmB at 37 °C results in the progressive decrease in the intensity of the reflectivity signal, suggesting incremental penetration of hydrogenous material in the deuterated lipid bilayer. Therefore, we proceeded from the assumption that the primary changes in the reflectivity originate from the penetration of PmB within the bilayer.

We set up the model to preserve most of the parameters obtained for the $_{dPL/dLPS}$OMM at 37 °C while integrating four additional parameters representing the volume fraction of intercalated PmB in the calculations for the SLD of the four layers, as well as allowing the hydration of the tail region and core OS to vary. The only additional structural parameter that was allowed to vary was the thickness of the core OS, which we had observed previously to change significantly after PmB addition.[18] The fits obtained for the two samples, one treated directly with 100 μg/mL (3a) and the other bilayer in the final state of the PmB titration (3b) yielded overall similar PmB penetration profiles across the membrane. In both samples PmB was found to be nearly absent in the core OS and localized predominantly in the lipid A region of LPS with lower amounts of PmB penetrating in the phospholipid tail region. PmB was also detected in the phospholipid headgroup regions, however, this region is the only nonperdeuterated part of the bilayer and therefore lacks sufficient contrasts with the antimicrobial to provide accurate data (Table 1). This is reflected in the significantly broader 68% confidence interval of the posterior distribution associated with the PmB volume fractions found in this region in both samples.

PmB penetration also resulted in a minor increase in the hydration of the tail region of the $_{dPL/dLPS}$OMM. Although negligible amounts of PmB were found to reside in the core OS region, the carbohydrate head groups of LPS were found to be ∼30% thinner and ∼25% more hydrated after the antimicrobial treatment. The scenario outlined by the modeled data clearly reveals a significant amount of PmB penetrating inside the membrane at 37 °C and localized predominantly in the lipid A hydrophobic region. Furthermore, the parameters obtained suggest that PmB hijacks LPS molecules from the bilayer, replacing the volume previously occupied by lipid A but not the volume left by the core OS that becomes primarily filled with water.

Finally, As a control for the sensitivity of the analysis to the presence of PmB in the bilayer, we fitted the data collected on the bilayer before the addition of the antimicrobial using the model that includes PmB volume fractions. The results show a small fitted PmB volume fraction in the deuterated regions of the bilayer, between ∼2 and ∼5%, with confidence intervals of the same magnitude of the fitted values (Figure S3). The marginalized posterior distribution for the PmB volume

https://doi.org/10.1021/acsomega.4c07648
ACS Omega 2025, 10, 2616−2627

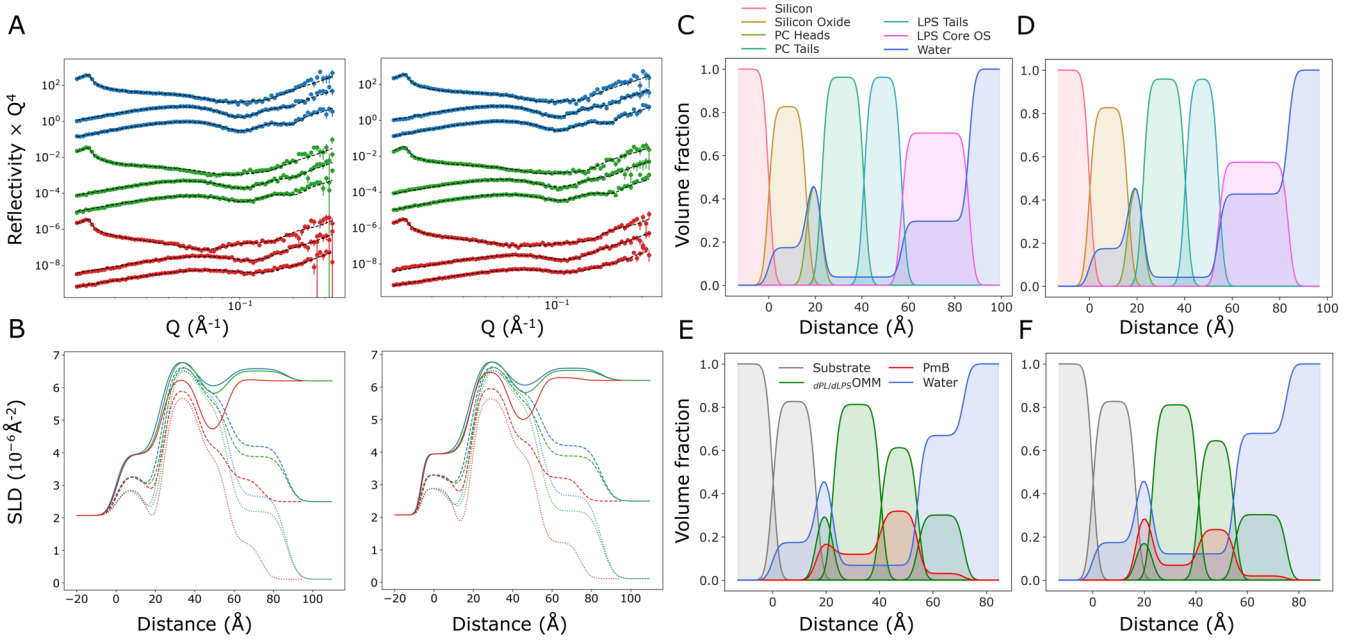

Figure 4. PmB localization in the OMM. (A) Neutron reflectivity data and fits of two $_{dPL/dLPS}$OMM measured in three solution isotopic contrasts at room temperature (blue), 37 °C (green), and 37 °C in the presence of 100 μg/mL PmB (red). The left panel corresponds to the sample that was heated to 37 °C and treated directly with 100 μg/mL PmB while the right panel corresponds to the sample that was heated to 37 °C and titrated with increasing amounts of PmB before reaching the final 100 μg/mL shown here. The global reduced χ^2 of the constrained fit is 2.77 (B) SLD profiles corresponding to the fits shown above each panel and following the same color coding as that in A. The green and blue curves on the left and on the right plots are mostly identical and only differ in the silicon oxide layer since the bilayer parameters were constrained to fit the same values as they describe the same sample structure prepared on two substrates. (C) Volume fraction profiles of the $_{dPL/dLPS}$OMM components at 20 °C (D), 37 °C, (E) 37 °C + 100 μg/mL PmB (direct 100 μg/mL PmB injection), and (F) 37 °C + 100 μg/mL PmB (last step of the titration sequence). The volume fractions plot in (E, F) correspond to the SLD profiles in red on the left and right plots in (B) respectively.

fraction in the three deuterated slabs is heavily skewed toward zero, indicating that the Bayesian error analysis tends to correctly minimize the presence of the antimicrobial when it is not physically present in the system. In the inner headgroup region, which is the only nonperdeuterated component of the bilayer, the fits are significantly less sensitive to the presence of the antimicrobial as shown by the spread-out posterior distribution. In this region, the SLDs of the lipopeptide and of the phospholipid headgroup are too similar to be accurately distinguished (Table 1).

4. DISCUSSION

As recently pointed out by Prasad et al., the pipeline for developing new antibiotics active against Gram-negative pathogens is extremely "leaky".[7] 62% of drug candidates in this category have been abandoned within 12 years of initiating the FDA investigational new drug application for new antibiotic candidates, while 43% of the 61 antibiotics approved between 1980 and 2009 were withdrawn due to safety concerns. In this scenario, the class of polymyxins, including polymyxins B and colistin, has played an important role in the fight against multidrug-resistant Gram-negative bacteria. Their clinical utility has been hampered by significant nephrotoxicity and neurotoxicity concerns, leading to an initial period of abandonment and then a resurgence as last-resort therapies. The recent development of safer and more effective polymyxin derivatives, such as SPR206, QPX9003, and MRX-8, discussed in detail in the recent review by Slingerland and Martin,[13] poses the accent on the progress made over the years in mitigating toxicity while improving activity of polymyxin analogues.

LPS−PmB interactions have been investigated by using various OM models that do not necessarily preserve lipid asymmetry but prioritize compositional accuracy over membrane architecture. One versatile approach involves the use of OM vesicles to mimic the bacterial surface. OM vesicles can be fused onto polymer-functionalized surfaces to create planar models of the OM, which have been investigated by QCMD.[35] More recently, entire OM vesicles have been immobilized and used to study the binding of PmB using SPR.[36] Top-down OM vesicle-based approaches and bottom-up layer-by-layer methods provide complementary strategies for investigating the response of the Gram-negative surface to antimicrobials. The top-down approach offers highly complex membranes and the advantage of higher throughput, while the bottom-up method provides unique structural insights by simplifying the system and allowing tracking of individual components.

An often overlooked aspect of the mechanism of action of PmB is the temperature dependence of its bactericidal effect.[15−17] Biophysical studies on PmB binding to LPS have consistently shown different thermodynamic behavior of the interaction above and below *E. coli* growth temperature, often coinciding with a human physiological temperature of 37 °C,[37] which correlated with LPS-mediated PmB resistance mechanisms.[38] We addressed these aspects in our previous work, showing that isotopically asymmetric $_{dPL/hLPS}$OMM provides a useful model system to investigate the temperature dependence of PmB-mediated disruption by combining isotope-sensitive structural information from NR and chemical data from Fourier transform infrared spectroscopy. Infrared spectroscopy revealed that both leaflets undergo a phase transition

https://doi.org/10.1021/acsomega.4c07648
ACS Omega 2025, 10, 2616−2627

with midpoints at distinct temperatures: 36 °C for h-LPS and 39 °C for d_{62}DPPC. Not only the midpoints of the transition temperatures of the two leaflets could be discriminated, but the overall trend of the transition indicates that synthetic d_{62}DPPC undergoes a sharp transition because of its chemical purity, while h-LPS shows a broader transition due to its more heterogeneous chemical structure. NR then provided temperature-dependent information on the perturbation of the asymmetric structure of the bilayer by PmB.[18]

In the present work we overcome one important limitation of $_{dPL/hLPS}$OMM which prevented us from localizing PmB within the OMM after its penetration. The hydrogenous RaLPS in the $_{dPL/hLPS}$OMM was substituted by its deuterium labeled counterpart to yield a fully deuterated $_{dPL/dLPS}$OMM, an approach proven successful with deuterated RcLPS by Gong et al.[39] This enabled the differentiation of the deuterated lipid components of the membrane from the hydrogenous volume fraction of PmB intercalated in each one of the four lipid bilayer regions to reveal its final distribution in the OMM (Figure 4, Table 1). We started by comparing the purified d-LPS produced in this study with commercial h-RaLPS from the *E. coli* EH100 strain used for the $_{dPL/hLPS}$OMM in our previous work. Both the polysaccharide moiety and the lipid A components of h- and d-LPS were shown to be indistinguishable by SDS PAGE and TLC respectively, despite the high level of deuteration of d-LPS revealed by IR, indicating no major differences in terms of LPS molecular weight and lipid A polarity (Figure 1b,c,e).

Reconstitution of d-LPS into $_{dPL/dLPS}$OMM yielded high-quality asymmetric lipid bilayers as established over several earlier studies on $_{dPL/hLPS}$OMM[18,25−27] and the high level of deuteration allowed us to increase the sensitivity of the measurement toward penetration of the hydrogenous antibiotic. The model-independent analysis quantified drug penetration as a function of concentration and temperature showing detectable effects down to antibiotic concentrations close to the minimum inhibitory concentration values reported for PmB, which range between 0.5 and 2 μg/mL for sensitive strains and between 4 and 128 μg/mL for resistant ones[40] (Figure 3b). Temperature was again confirmed to be a critical factor for PmB penetration showing an all-or-none response at 20 and 37 °C (Figures 2c, 3a, and 5). The temperature ramp in the presence of the antibiotic highlighted the steep transition of the reflectivity signal around ∼32 °C. In our previous work using isotopically asymmetric models containing nondeuterated LPS, we observed the same transition but shifted to ∼36 °C.[18] This is in excellent agreement with the predicted lower melting point of tail-deuterated lipids compared to their hydrogenous counterparts which is known to be ∼4 °C lower.[41] For comparison the melting point of DPPC is ∼42 °C, while that of its tail-deuterated analogue is ∼38 °C.

We chose the temperature of 37 °C for the structural characterization because it corresponds to the growth temperature of *E. coli* and human physiological temperature. Given the difference in melting temperature of h-LPS and d-LPS, at 37 °C we expect a lower degree of PmB penetration in the hydrogenous LPS compared to the deuterated LPS due to the higher transition temperature of the former. At 36 °C and in the presence of PmB, a comparison between the models containing h-LPS and d-LPS shows that the membrane containing h-LPS is midway through the disruption process,[18] whereas for d-LPS, structural changes are beyond the midpoint and closer to completion.

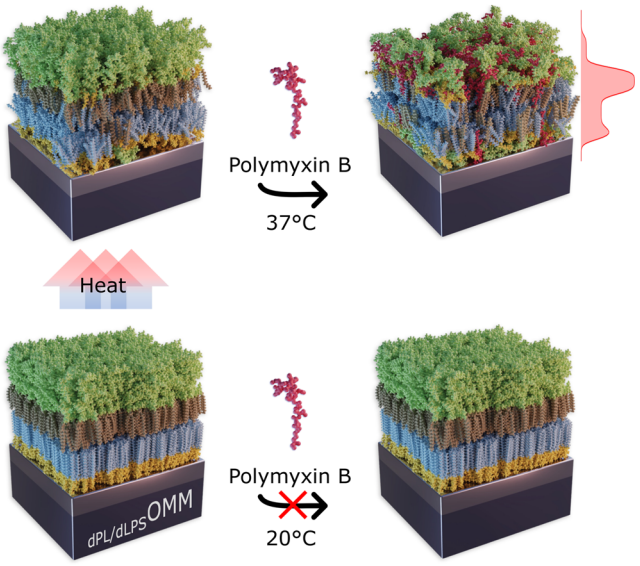

Figure 5. Schematic representation of the depth-resolved temperature-dependent penetration of PmB in the $_{dPL/dLPS}$OMM.

These results point once again to the importance of the phase transition of LPS to a more fluid phase around the temperature at which *E. coli* is grown. Recent reports on the diffusion coefficient of LPS in *E. coli* grown at ∼37 °C have shown a reduction in diffusivity of 7 times when the cells were cooled at ∼20 °C, indicating a significant alteration of membrane fluidity in this range of temperatures.[42] Interestingly, Ginez et al. showed that LPS diffusivity remains constant in cells grown at 20, 30, and 37 °C when measured at the growth temperature, but is significantly altered when temperature is shifted above and below growth temperature after the cells reach stationary phase. This was observed for *E. coli* strain MG1655, which produces RaLPS and is a derivative of the BW25113 strain used here to produce d-LPS. The authors also performed experiments directly on BW25113 showing that LPS diffusivity overlaps between the two strains.[42] Further evidence for the importance of homeoviscous adaptation of LPS in the OM and its role in resisting PmB effects comes from the altered acylation of lipid A in *Francisella novicida* grown at different temperatures. Lower-melting C16 acyl chains are added to lipid A when grown at low temperatures (18 °C) while at 37 °C LPS contains mainly higher-melting C18 chains. While inhibiting the expression of the C18 transferring enzyme resulted in a ∼2.5 increase in PmB susceptibility compared to WT, inhibiting the C16 transferring enzyme resulted in strains ∼13.5 times more resistant than WT to PmB.[43] Resistance against polymixins is mediated by LPS modifications that either alter its charge or acylation state.[44] The former are aimed at reducing the overall negative charge on LPS to weaken the binding of the cationic lipopeptide, and the latter reinforces the hydrophobic interior of the OM by altering the acylation state of LPS,[45] with an interplay existing between the two mechanisms.[46] The results shown here suggest that the mechanism of resistance mediated by altering LPS acylation would result in a higher phase transition temperature and afford protection by providing tighter lipid packing of the lipid A acyl chains. A relevant difference between the rough LPS used here and that of wild-type organisms is the presence of O-antigen polysaccharide chains in the latter, which offer protection against environmental

https://doi.org/10.1021/acsomega.4c07648
ACS Omega 2025, 10, 2616−2627

threats, including PmB[47] Thus, model membranes with smooth LPS and long O-antigen chains are expected to show lower sensitivity to PmB penetration, a topic we plan to explore in future studies.

In order to track the penetration of PmB in the $_{dPL/dLPS}$OMM we performed a constrained fit of 18 reflectivity curves to reduce the total number of free parameters and obtain information on the effect of temperature on the OMM structure as well as the volume fraction distribution of PmB in the lipid bilayer. Table 1c displays the volume fractions of PmB in the four regions of the OMM bilayer obtained from the average of the two independent samples. The highest PmB amount accumulated in the lipid A region of the OMM, amounting to 27.5 ± 2.5% of the molecular volume of the layer, with further penetration in the inner DPPC leaflet. Negligible amounts of PmB remained in the core OS region which displayed an increase in hydration and decrease in thickness pointing toward the partial removal of LPS molecules which is compatible with the scenario where PmB hijacks the lipid A component in the hydrophobic region of the OMM but does not fill the voids in the core OS region, leaving an increased water volume fraction and partially collapsed carbohydrates chains. A coherent picture of the effects of PmB on the OM is still lacking and even quite recently the interpretation of results obtained on the effects of PmB on the OM[48] have sparked a lively debate in the community.[49,50] In particular there seems to be no agreement on whether PmB induces fluidification[42,51,52] or rigidification[48,53] of the OM. Recent developments in high-resolution AFM of living bacteria show that the OM displays macroscopic phase separation between regions enriched in porins and LPS-rich regions which might be affected differently by PmB, providing a possible explanation for the discrepancies of the effects reported.[54] Specifically, since Ca^{2+} ions play a key role in stabilizing both LPS−LPS and LPS−porin interactions,[26,55] the discrepancies in the reported changes in the OM physical properties may stem from differences in the type of interaction being predominantly affected by PmB as well as the specific regions of the membrane being probed.

There has been extensive work using MD simulations on the interaction of PmB with in silico models of the Gram-negative cell envelope, recently reviewed by Weerakoon et al.[56] While MD could provide the atomic-level details to aid interpretation of the results, one of the outcomes highlighted by the authors is that in both atomistic and coarse-grained MD simulations it has been particularly difficult to sample insertion of PmB in the hydrophobic region of LPS due to the long time scales of its diffusion. MD simulations tend to overestimate the permanence of PmB in the inner core OS region where electrostatic interactions are strongest, while over more realistic time scales, these might be largely transient states preceding PmB insertion in the OM. Electrostatic interactions take place in the inner core region where the LPS anionic groups reside and this is where PmB gets usually stuck in simulations, in the proximity of RaLPS heptose sugars.[57] Further penetration is likely driven by hydrophobic forces which depend much more heavily on acyl chain dynamics which for LPS is notably slower than for phospholipids membranes.[42,58] In all of the simulations of PmB−LPS interactions reviewed, penetration of PmB in the hydrophobic core of LPS is accompanied by an increase in free energy, indicating a discrepancy with the self-promoted uptake mechanism proposed for the lipopeptide, and the membrane penetration observed *in vivo* and *in vitro* for PmB. We believe the all-or-none temperature-dependent response of PmB we identified using the model *in vitro* membranes would be an ideal test case for simulation force fields, providing a simple but clear benchmark for realistic OM *in silico* models.

5. CONCLUSIONS

By using perdeuterated asymmetric lipid bilayers that mimic the outer membrane of Gram-negative bacteria, we were able to track the penetration of the last-resort drug polymyxin B within the phospholipids and LPS layers, obtaining molecular-level structural information on a key step of the mechanism of action of a last-resort antibiotic. The temperature-dependent effects of PmB reported in our previous study[18] were confirmed and complemented by a new deuteration scheme providing further evidence for the critical role of LPS fluidity in the penetration of the antibiotic. The combination of model-dependent and model-independent analysis provided a robust and coherent picture of the scattering data, reducing the inherent bias that comes with relying on modeling alone, allowing us to comprehensively describe the antibiotic's effect in detail. We quantitatively determined the final composition of the membrane, including the antibiotic volume fraction across the sample as well as concentration and temperature effects. This approach can be extended to antimicrobial peptides targeted against Gram-negative pathogens including but not limited to novel polymyxin B derivatives and other membrane-active antibiotics.

■ ASSOCIATED CONTENT

Supporting Information

The Supporting Information is available free of charge at https://pubs.acs.org/doi/10.1021/acsomega.4c07648.

FTIR comparison of hydrogenous and tail-deuterated DPPC; corner plot of the posterior distributions from the NR error analysis; analysis of model sensitivity to the presence of PmB (PDF)

■ AUTHOR INFORMATION

Corresponding Author

Nicoló Paracini − *Institut Laue-Langevin, Large Scale Structures Group, Grenoble 38000, France;* orcid.org/0000-0003-3178-4867; Email: paracini@ill.eu,nicolo.paracini@ess.eu

Authors

Jeremy H. Lakey − *Biosciences Institute, Faculty of Medical Sciences, Newcastle University, Newcastle upon Tyne NE2 4HH, U.K.;* orcid.org/0000-0003-4646-9085

Luke A. Clifton − *ISIS Pulsed Neutron and Muon Source, Rutherford Appleton Laboratory, Oxford OX11 0QX, U.K.;* orcid.org/0000-0001-8754-362X

Complete contact information is available at: https://pubs.acs.org/10.1021/acsomega.4c07648

Notes

The authors declare no competing financial interest.

■ ACKNOWLEDGMENTS

This work was supported by ISIS beam time award RB1900032. N.P. was supported by a Facility Development Studentship funded by STFC, Newcastle University and OJ Bio Ltd. The authors are grateful to Dr. Helen Waller for her

support during deuterated LPS purification. LAC acknowledges Dr. Maximilian Skoda for helpful discussions. NP acknowledges Dr. Andrew Nelson for helpful advice on the refnx package.

■ ABBREVIATIONS

OMM: outer membrane model
PmB: polymyxin B
LPS: lipopolysaccharide
SLD: scattering length density
NR: neutron reflectometry
IR: infrared spectroscopy

■ REFERENCES

(1) Tommasi, R.; Brown, D. G.; Walkup, G. K.; Manchester, J. I.; Miller, A. A. ESKAPEing the labyrinth of antibacterial discovery. *Nat. Rev. Drug Discovery* **2015**, *14*, 529−542.
(2) Nikaido, H. Molecular basis of bacterial outer membrane permeability revisited. *Microbiol. Mol. Biol. Rev.* **2003**, *67*, 593−656.
(3) Henderson, J. C.; Zimmerman, S. M.; Crofts, A. A.; Boll, J. M.; Kuhns, L. G.; Herrera, C. M.; Trent, M. S. The Power of Asymmetry: Architecture and Assembly of the Gram-Negative Outer Membrane Lipid Bilayer. *Annu. Rev. Microbiol.* **2016**, *70*, 255−278.
(4) Di Lorenzo, F.; Duda, K. A.; Lanzetta, R.; Silipo, A.; De Castro, C.; Molinaro, A. A Journey from Structure to Function of Bacterial Lipopolysaccharides. *Chem. Rev.* **2022**, *122* (20), 15767−15821.
(5) Paracini, N.; Schneck, E.; Imberty, A.; Micciulla, S. Lipopolysaccharides at Solid and Liquid Interfaces: Models for Biophysical Studies of the Gram-negative Bacterial Outer Membrane. *Adv. Colloid Interface Sci.* **2022**, *301*, No. 102603.
(6) Sabnis, A.; Edwards, A. M. Lipopolysaccharide as an antibiotic target. *Biochim. Biophys. Acta, Mol. Cell Res.* **2023**, *1870*, No. 119507.
(7) Prasad, N. K.; Seiple, I. B.; Cirz, R. T.; Rosenberg, O. S. Leaks in the Pipeline: a Failure Analysis of Gram-Negative Antibiotic Development from 2010 to 2020. *Antimicrob. Agents Chemother.* **2022**, *66* (5), e00054-22.
(8) Zhao, J.; Cochrane, C. S.; Najeeb, J.; et al. Preclinical safety and efficacy characterization of an LpxC inhibitor against Gram-negative pathogens. *Sci. Transl. Med.* **2023**, *15* (708), eadf5668.
(9) Zampaloni, C.; Mattei, P.; Bleicher, K.; et al. A novel antibiotic class targeting the lipopolysaccharide transporter. *Nature* **2024**, *625* (7995), 566−571.
(10) Pahil, K. S.; Gilman, M. S. A.; Baidin, V.; Clairfeuille, T.; Mattei, P.; Bieniossek, C.; Dey, F.; Muri, D.; Baettig, R.; Lobritz, M.; Bradley, K.; Kruse, A. C.; Kahne, D. A new antibiotic traps lipopolysaccharide in its intermembrane transporter. *Nature* **2024**, *625* (7995), 572−577.
(11) Velkov, T.; Roberts, K. D.; Nation, R. L.; Thompson, P. E.; Li, J. Pharmacology of polymyxins: new insights into an 'old' class of antibiotics. *Fut. Microbiol.* **2013**, *8*, 711−724.
(12) Johnson, M. D.; Nation, R. L.; Li, J. *Antimicrobial Drug Resistance*; Springer International Publishing: Cham, 2017; pp 333−344.
(13) Slingerland, C. J.; Martin, N. I. Recent Advances in the Development of Polymyxin Antibiotics: 2010−2023. *ACS Infect. Dis.* **2024**, *10*, 1056−1079.
(14) Ledger, E. V. K.; Sabnis, A.; Edwards, A. M. Polymyxin and lipopeptide antibiotics: membrane-targeting drugs of last resort. *Microbiology* **2022**, *168*, 001136.
(15) Hodate, K.; Bito, Y. Temperature dependence of bactericidal action of polymyxin B. *Microbiol. Immunol.* **1982**, *26*, 737−740.
(16) Katsu, T.; Yoshimura, S.; Tsuchiya, T.; Fujita, Y. Temperature Dependence of Action of Polymyxin B on *Escherichia coli*1. *J. Biochem.* **1984**, *95*, 1645−1653.
(17) Teubner, M.; Bader, J. Resistance to polymyxin B at low temperature: A function of the outer membrane in gram-negative bacteria. *FEMS Microbiol. Lett.* **1977**, *1*, 75−77.
(18) Paracini, N.; Clifton, L. A.; Skoda, M. W. A.; Lakey, J. H. Liquid crystalline bacterial outer membranes are critical for antibiotic susceptibility. *Proc. Natl. Acad. Sci. U.S.A.* **2018**, *115*, No. 201803975.
(19) Clifton, L. A.; Hall, S. C.; Mahmoudi, N.; Knowles, T. J.; Heinrich, F.; Lakey, J. H. Structural investigations of protein−lipid complexes using neutron scattering. *Lipid-Protein Interact.: Methods Prot.* **2019**, *2003*, 201−251.
(20) Paracini, N.; Clifton, L. A.; Lakey, J. H. Studying the surfaces of bacteria using neutron scattering: finding new openings for antibiotics. *Biochem. Soc. Trans.* **2020**, *48*, 2139−2149.
(21) Meilleur, F.; Weiss, K. L.; Myles, D. A. In *Micro and Nano Technologies in Bioanalysis: Methods and Protocols*, 544th ed.; Foote, R. S.; Lee, J. W., Eds.; Springer: New York, 2009; pp 281−292.
(22) Galanos, C.; Lüderitz, O.; Westphal, O. A new method for the extraction of R lipopolysaccharides. *Eur. J. Biochem.* **1969**, *9*, 245−249.
(23) Laemmli, U. K. Cleavage of Structural Proteins during the Assembly of the Head of Bacteriophage T4. *Nature* **1970**, *227*, 680−685.
(24) Fomsgaard, A.; Freudenberg, M. A.; Galanos, C. Modification of the silver staining technique to detect lipopolysaccharide in polyacrylamide gels. *J. Clin. Microbiol.* **1990**, *28*, 2627−2631.
(25) Clifton, L. A.; Skoda, M. W. A.; Daulton, E. L.; Hughes, A. V.; Le Brun, A. P.; Lakey, J. H.; Holt, S. A. Asymmetric phospholipid: lipopolysaccharide bilayers; a Gram-negative bacterial outer membrane mimic. *J. R. Soc. Interface* **2013**, *10*, No. 20130810.
(26) Clifton, L. A.; Skoda, M. W. A.; Le Brun, A. P.; Ciesielski, F.; Kuzmenko, I.; Holt, S.; Lakey, J. H. The Effect of Divalent Cation Removal on the Structure of Gram-negative Bacterial Outer Membrane Models. *Langmuir* **2015**, *31*, 404−412.
(27) Clifton, L. A.; Ciesielski, F.; Skoda, M. W. A.; Paracini, N.; Holt, S. A.; Lakey, J. H. The Effect of Lipopolysaccharide Core Oligosaccharide Size on the Electrostatic Binding of Antimicrobial Proteins to Models of the Gram Negative Bacterial Outer Membrane. *Langmuir* **2016**, *32*, 3485−3494.
(28) Arnold, O.; Bilheux, J.; Borreguero, J.; et al. Mantid - Data analysis and visualization package for neutron scattering and μ SR experiments. *Nucl. Instrum. Methods Phys. Res., Sect. A* **2014**, *764*, 156−166.
(29) Nelson, A. R. J.; Prescott, S. W. refnx: neutron and X-ray reflectometry analysis in Python. *J. Appl. Crystallogr.* **2019**, *52*, 193−200.
(30) Paracini, N. Refnx Jupyter Notebook for NR Analysis of PmB-dLPS 2024 https://github.com/paracini/refnx_models/blob/main/18_contrasts_dRaLPS_RT_37C_PmB.ipynb. (accessed on June 29, 2024).
(31) Paracini, N. Refnx Jupyter Notebook and Datasets for NR Analysis of PmB-dLPS 2024 https://zenodo.org/records/14209698. (accessed on Nov 24, 2024).
(32) Armen, R. S.; Uitto, O. D.; Feller, S. E. Phospholipid component volumes: determination and application to bilayer structure calculations. *Biophys. J.* **1998**, *75*, 734−744.
(33) Whitfield, C.; Williams, D. M.; Kelly, S. D. Lipopolysaccharide O-antigens-bacterial glycans made to measure. *J. Biol. Chem.* **2020**, *295*, 10593−10609.
(34) Gerelli, Y. Phase Transitions in a Single Supported Phospholipid Bilayer: Real-Time Determination by Neutron Reflectometry. *Phys. Rev. Lett.* **2019**, *122*, No. 248101.
(35) Hsia, C.-Y. Y.; Chen, L.; Singh, R. R.; DeLisa, M. P.; Daniel, S. A Molecularly Complete Planar Bacterial Outer Membrane Platform. *Sci. Rep.* **2016**, *6*, No. 32715.
(36) Buchholz, K. R.; Reichelt, M.; Johnson, M. C.; Robinson, S. J.; Smith, P. A.; Rutherford, S. T.; Quinn, J. G. Potent activity of polymyxin B is associated with long-lived super-stoichiometric accumulation mediated by weak-affinity binding to lipid A. *Nat. Commun.* **2024**, *15*, No. 4733.
(37) Brandenburg, K.; David, A.; Howe, J.; Koch, M. H. J.; Andrä, J.; Garidel, P. Temperature dependence of the binding of endotoxins to

https://doi.org/10.1021/acsomega.4c07648
ACS Omega 2025, 10, 2616−2627

the polycationic peptides polymyxin B and its nonapeptide. *Biophys. J.* **2005**, *88*, 1845−1858.
(38) Howe, J.; Andrä, J.; Conde, R.; Iriarte, M.; Garidel, P.; Koch, M. H. J.; Gutsmann, T.; Moriyón, I.; Brandenburg, K. Thermodynamic analysis of the lipopolysaccharide-dependent resistance of gram-negative bacteria against polymyxin B. *Biophys. J.* **2007**, *92*, 2796−2805.
(39) Gong, H.; Hu, X.; Liao, M.; Fa, K.; Ciumac, D.; Clifton, L. A.; Sani, M.-A.; King, S. M.; Maestro, A.; Separovic, F.; Waigh, T. A.; Xu, H.; McBain, A. J.; Lu, J. R. Structural Disruptions of the Outer Membranes of Gram-Negative Bacteria by Rationally Designed Amphiphilic Antimicrobial Peptides. *ACS Appl. Mater. Interfaces* **2021**, *13*, 16062−16074.
(40) Chew, K. L.; La, M.-V.; Lin, R. T. P.; Teo, J. W. P. Colistin and Polymyxin B Susceptibility Testing for Carbapenem-Resistant and mcr -Positive Enterobacteriaceae: Comparison of Sensititre, MicroScan, Vitek 2, and Etest with Broth Microdilution. *J. Clin. Microbiol.* **2017**, *55*, 2609−2616.
(41) Bryant, G.; Taylor, M. B.; Darwish, T. A.; Krause-Heuer, A. M.; Kent, B.; Garvey, C. J. Effect of deuteration on the phase behaviour and structure of lamellar phases of phosphatidylcholines - Deuterated lipids as proxies for the physical properties of native bilayers. *Colloids Surf., B* **2019**, *177*, 196−203.
(42) Ginez, L. D.; Osorio, A.; Vázquez-Ramírez, R.; Arenas, T.; Mendoza, L.; Camarena, L.; Poggio, S. Changes in fluidity of the *E. coli* outer membrane in response to temperature, divalent cations and polymyxin-B show two different mechanisms of membrane fluidity adaptation. *FEBS J.* **2022**, *289*, 3550−3567.
(43) Li, Y.; Powell, D. A.; Shaffer, S. A.; Rasko, D. A.; Pelletier, M. R.; Leszyk, J. D.; Alison, J.; Masoudi, A.; Goodlett, D. R.; Wang, X.; Radulescu, A.; Ernst, R. K.; Scott, A. J. Correction for Li et al., LPS remodeling is an evolved survival strategy for bacteria. *Proc. Natl. Acad. Sci. U.S.A.* **2012**, *109*, 13877.
(44) Needham, B. D.; Trent, M. S. Fortifying the barrier: the impact of lipid A remodelling on bacterial pathogenesis. *Nat. Rev. Microbiol.* **2013**, *11*, 467−481.
(45) Boll, J. M.; Tucker, A. T.; Klein, D. R.; Beltran, A. M.; Brodbelt, J. S.; Davies, B. W.; Trent, M. S. Reinforcing lipid a acylation on the cell surface of acinetobacter baumannii promotes cationic antimicrobial peptide resistance and desiccation survival. *MBio* **2015**, *6*, 10−1128.
(46) Tran, A. X.; Lester, M. E.; Stead, C. M.; Raetz, C. R. H.; Maskell, D. J.; McGrath, S. C.; Cotter, R. J.; Trent, M. S. Resistance to the antimicrobial peptide polymyxin requires myristoylation of *Escherichia coli* and Salmonella typhimurium lipid A. *J. Biol. Chem.* **2005**, *280*, 28186−28194.
(47) Lindell, K.; Fahlgren, A.; Hjerde, E.; Willassen, N.-P.; Fällman, M.; Milton, D. L. Lipopolysaccharide O-Antigen Prevents Phagocytosis of Vibrio anguillarum by Rainbow Trout (Oncorhynchus mykiss) Skin Epithelial Cells. *PLoS One* **2012**, *7*, No. e37678.
(48) Manioglu, S.; Modaresi, S. M.; Ritzmann, N.; Thoma, J.; Overall, S. A.; Harms, A.; Upert, G.; Luther, A.; Barnes, A. B.; Obrecht, D.; Müller, D. J.; Hiller, S. Antibiotic polymyxin arranges lipopolysaccharide into crystalline structures to solidify the bacterial membrane. *Nat. Commun.* **2022**, *13*, 6195 DOI: 10.1038/s41467-022-33838-0.
(49) Manioglu, S.; Modaresi, S. M.; Thoma, J.; et al. Antibiotics and hexagonal order in the bacterial outer membrane. *Nat. Commun.* **2023**, *14*, 4773.
(50) Manioglu, S.; Modaresi, S. M.; Thoma, J.; Overall, S. A.; Upert, G.; Luther, A.; Barnes, A. B.; Obrecht, D.; Müller, D. J.; Hiller, S. Reply to: Antibiotics and hexagonal order in the bacterial outer membrane. *Nat. Commun.* **2023**, *14* (1), 4773.
(51) Brandenburg, K.; Arraiza, M. D.; Lehwark-Ivetot, G.; Moriyon, I.; Zähringer, U. The interaction of rough and smooth form lipopolysaccharides with polymyxins as studied by titration calorimetry. *Thermochim. Acta* **2002**, *394*, 53−61.
(52) Fu, L.; Wan, M.; Zhang, S.; Gao, L.; Fang, W. Polymyxin B Loosens Lipopolysaccharide Bilayer but Stiffens Phospholipid Bilayer. *Biophys. J.* **2020**, *118*, 138−150.
(53) Jefferies, D.; Hsu, P. C.; Khalid, S. Through the Lipopolysaccharide Glass: A Potent Antimicrobial Peptide Induces Phase Changes in Membranes. *Biochemistry* **2017**, *56*, 1672−1679.
(54) Benn, G.; Mikheyeva, I. V.; Inns, P. G.; Forster, J. C.; Ojkic, N.; Bortolini, C.; Ryadnov, M. G.; Kleanthous, C.; Silhavy, T. J.; Hoogenboom, B. W. Phase separation in the outer membrane of *Escherichia coli*. *Proc. Natl. Acad. Sci. U.S.A.* **2021**, *118*, No. e2112237118.
(55) Arunmanee, W.; Pathania, M.; Solovyova, A. S.; Le Brun, A. P.; Ridley, H.; Baslé, A.; van den Berg, B.; Lakey, J. H. Gram-negative trimeric porins have specific LPS binding sites that are essential for porin biogenesis. *Proc. Natl. Acad. Sci. U.S.A.* **2016**, *113*, No. 201602382.
(56) Weerakoon, D.; Petrov, K.; Pedebos, C.; Khalid, S. Polymyxin B1 within the *E. coli* cell envelope: insights from molecular dynamics simulations. *Biophys. Rev.* **2021**, *13*, 1061−1070.
(57) Jiang, X.; Sun, Y.; Yang, K.; Yuan, B.; Velkov, T.; Wang, L.; Li, J. Coarse-grained simulations uncover Gram-negative bacterial defense against polymyxins by the outer membrane. *Comput. Struct. Biotechnol. J.* **2021**, *19*, 3885−3891.
(58) Sun, J.; Rutherford, S. T.; Silhavy, T. J.; Huang, K. C. Physical properties of the bacterial outer membrane. *Nat. Rev. Microbiol.* **2022**, *20*, 236−248.

NOTE ADDED AFTER ASAP PUBLICATION

This paper was published January 14, 2025. An update has been made in the first paragraph of the Introduction. The revised version was reposted on January 16, 2025.

https://doi.org/10.1021/acsomega.4c07648
ACS Omega 2025, 10, 2616−2627